Thermo X
https://doi.org/10.70401/tx.2026.0020

Supplementary information

Imaging thermal properties of thermal interface materials using frequency-domain thermoreflectance microscopy

Yuhan Yao, Haobo Yang, Ronggui Yang, Xin Qian

S1.SEM and the Corresponding EDS Images of the TIM

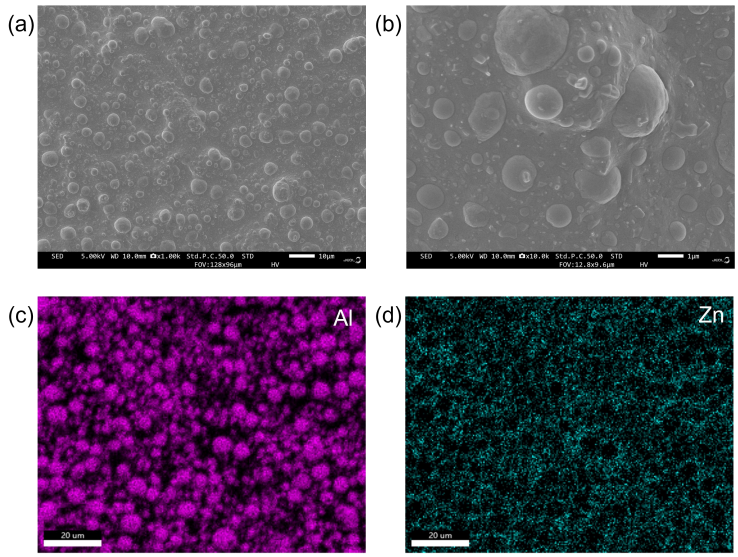

Figure S1. (a-b) SEM and (c-d) EDS images of the TIM, consisting of micron-sized Al_2O_3 particles and ZnO nanoparticles dispersed in a PDMS matrix. SEM: Scanning electron microscopy; EDS: energy dispersive spectroscopy; TIM: thermal interface material; PDMS: polydimethylsiloxane.

S2.Contact Pressure Measurement and Bondline Thickness Characterization

The contact pressure applied by the fixture was controlled by four spring-loaded screws and measured using a force sensor placed between the substrate and the fixture clamp. The contact pressure was approximately 36 psi, calculated by dividing the measured force (24.59 N) by the contact area of the TIM (100 mm^2). Figure S2a shows the measured force. The bondline thickness (BLT) of the TIM layer was extracted from micro-CT cross-sectional images. Figure S2b. shows a representative CT cross-section of the TIM. The measured BLT is approximately 12.8 µm, and the thickness is uniform across the imaging area.

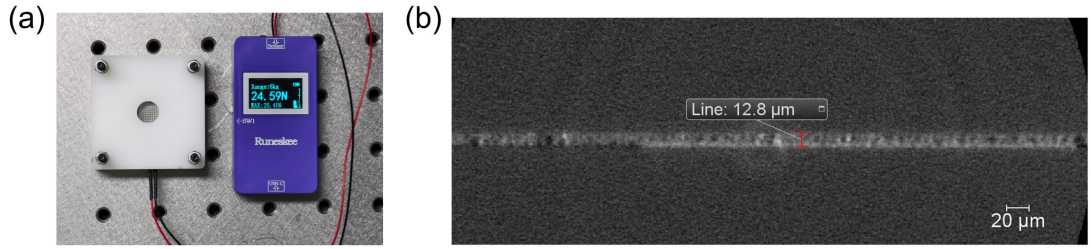

Figure S2. (a) Photograph of the contact pressure measurement setup and the measured contact pressure; (b) Micro-CT cross-sectional image showing the bondline thickness of the TIM layer. CT: computed tomography.

S3.The Customized Fixture

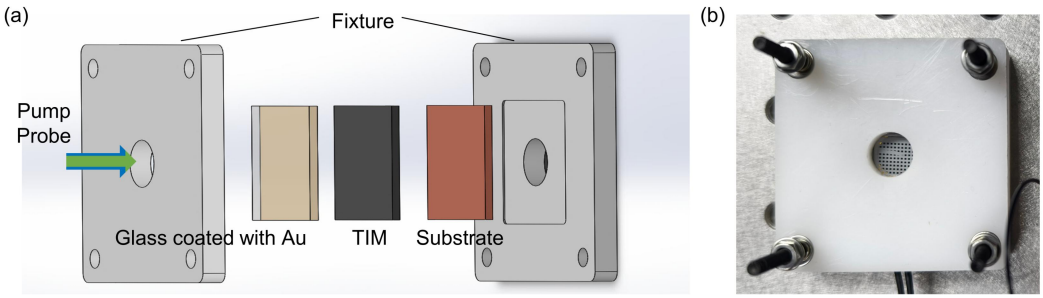

Figure S3. (a) Schematic diagram of the fixture assembly; (b) Photograph of the actual fixture. The TIM is sandwiched between a transducer-coated glass slide and a substrate wafer and secured with the fixture. TIM: thermal interface material.

S4.Calibration of Experimental Control Parameters

The thermal conductivity of the gold transducer was obtained by measuring the electrical conductivity via the four-point probe method and converting it to thermal conductivity using the Wiedemann–Franz law ($k_{\mathrm{Au}} = LT\sigma$), with the Lorenz number L = 2.44 × 10^{-8} W Ω K^{-2}, yielding k_{Au} = 250 W m^{-1} K^{-1}. The thickness of the gold transducer d_{Au} was calibrated by a profilometer. The silica substrate's thermal conductivity $k_{\mathrm{SiO_2}}$ and the gold-glass interfacial thermal conductance $G_{\mathrm{SiO_2}}$ were pre-determined using FDTR as known parameters. The thermal conductivity and volumetric heat capacity of the TIM are adopted from the manufacturer's specifications. The pump and probe laser spot radii are both 1.6 μm, which is the typical spot size achieved with a 20× objective. The control parameters are summarized in Table S1, which are used for data reduction and sensitivity analysis.

Table S1. Input parameters for the sensitivity analysis include thickness d, thermal conductivity k, volumetric heat capacity C and interface thermal conductance G.

	d	k	C	G
Units	nm	W m^{-1} K^{-1}	MJ m^{-3} K^{-1}	MW m^{-2} K^{-1}
Glass	1 × 10^{6}	1.4[1]	1.65[2]	/
Interface 1	/	/	/	42.9
Au	110	250	2.48[3]	/
Interface 2	/	/	/	30
TIM	1.28 × 10^{4}	13.8	2.11	/

S5.Spatial Co-Registration Between FDTR Mapping and Micro-CT Imaging

To correlate the FDTR thermal-property maps with the microstructure observed by micro-CT, spatial co-registration was performed on the same sandwiched TIM sample. During sample preparation, the gold transducer was deposited through a square shadow mask, producing a square-patterned gold film with sharp edges that served as markers for spatial alignment. Before FDTR mapping, the sample was rotated so that the XY scanning axes were aligned with the edges of the patterned gold transducer. The FDTR mapping region was then selected by positioning the piezo translation stage such that the scanning boundaries coincided with the gold-film boundaries, as shown in Figure S4a.

After FDTR measurement, micro-CT imaging was performed on the same assembled sample. The patterned gold transducer was clearly visible in the CT images due to the high X-ray attenuation of gold. Therefore, the CT slices and FDTR maps could be aligned using the gold-film edges as common references, as shown in Figure S4b. The corresponding FDTR amplitude image is shown in Figure S4c, where the mapped region is defined in the same coordinate frame.

Since the positioning accuracy of the piezo translation stage can reach ~20 nm, the uncertainty associated with FDTR stage positioning is much smaller than the characteristic length scale of the mapped features. The spatial co-registration uncertainty is therefore mainly limited by the micro-CT voxel size of 0.6 μm. Based on this alignment procedure, the high- and low-conductivity regions identified in the FDTR maps can be correlated with the corresponding microstructural features observed in the micro-CT images.

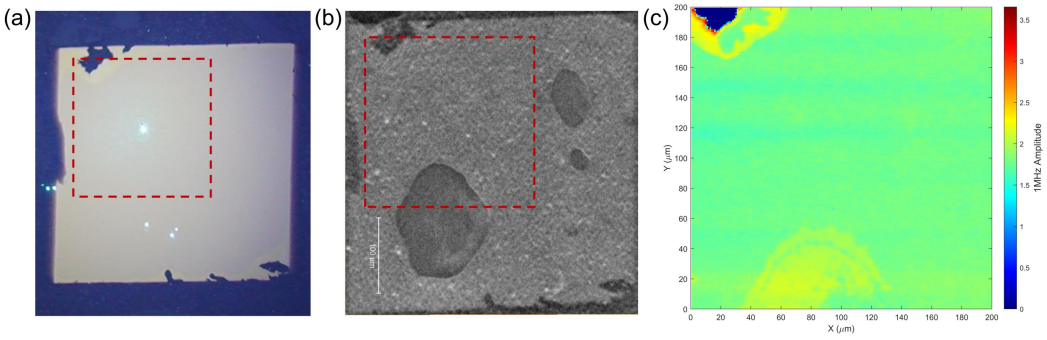

Figure S4. (a) Optical image and (b) corresponding micro-CT slice of the square-patterned gold transducer on the sandwiched TIM sample. The red dashed box indicates the region selected for FDTR mapping; (c) FDTR amplitude image measured at 1 MHz. CT: computed tomography; TIM: thermal interface material; FDTR: frequency-domain thermoreflectance.

S6.Thermal Property Evolution Under Varying Contact Pressures

This section provides additional details supporting the pressure-dependent results shown in the main text. We first describe the spatial alignment procedure used to compare thermal-property maps obtained at different pressures. We then present the full thermal-property maps and statistical distributions of the thermal grease during loading and unloading. Finally, pressure-dependent measurements on a commercial thermal pad are provided to demonstrate the applicability of the method to soft solid TIMs.

S6.1 Spatial alignment of pressure-dependent FDTR maps

To compare the thermal-property maps measured under different contact pressures, spatial alignment was performed during both the FDTR scanning process and the post-processing stage. During measurement, the sample orientation was adjusted so that the FDTR scanning directions were parallel to the edges of the patterned gold transducer. Distinct features on the gold film, such as film corners, edge irregularities, or local defects, were selected as reference points to define the scanning origin. This procedure ensured that the mapped regions under different pressures were located in approximately the same area of the sample.

After the measurements, the maps obtained at different pressures were further registered using the reflectivity images recorded during FDTR scanning. As shown in Figure S5a, the reflectivity images contain identifiable features from the gold film, which were used as fiducial markers for image registration. The thermal-property maps were shifted according to these features and then cropped to the common overlapping region, yielding the spatially aligned datasets shown in Figure S5b. This procedure minimizes the influence of small lateral sample shifts caused by pressure adjustment and enables direct comparison of local thermal features during loading and unloading.

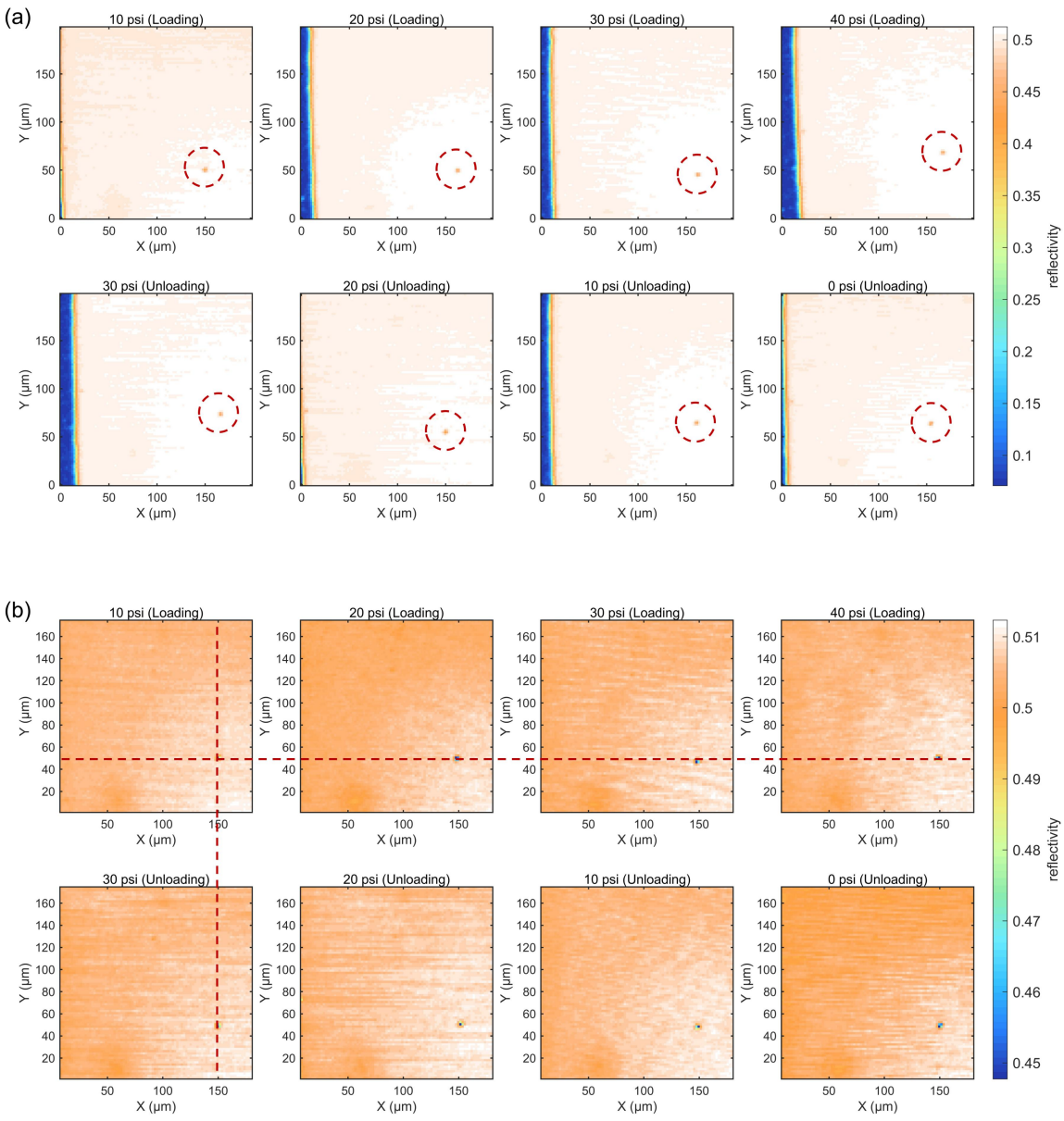

Figure S5. (a) Reflectivity images recorded during FDTR scanning under different contact pressures. Red circles indicate the alignment markers; (b) Aligned and cropped thermal-property maps obtained after shifting the datasets according to the fiducial features in the reflectance images. FDTR: frequency-domain thermoreflectance.

S6.2 Pressure-dependent thermal-property maps of thermal grease

The co-registered thermal-conductivity and interfacial thermal conductance maps of the thermal grease under different contact pressures are shown in Figure S6a,b, respectively.

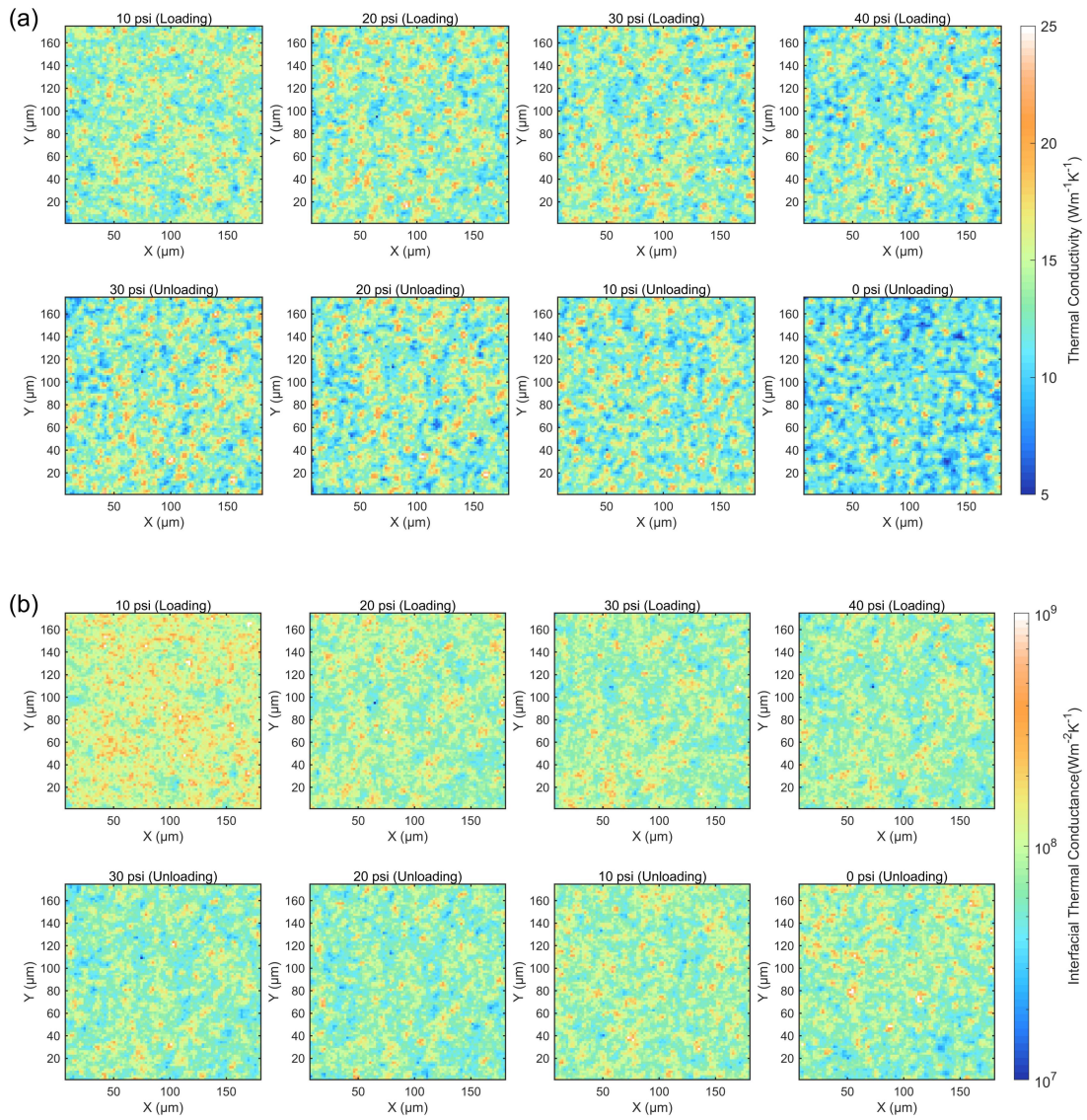

Figure S6. (a) Thermal conductivity and (b) interfacial thermal conductance maps of thermal grease at different contact pressures during loading and unloading processes.

S6.3 Pressure-dependent FDTR imaging of thermal pad

To examine whether the pressure-dependent FDTR imaging approach can be extended to other types of TIMs, we also performed measurements on a commercial thermal pad (Tflex HD90000). Unlike thermal grease, the thermal pad is a soft solid TIM with a more stable macroscopic shape and lower flowability.

The pressure-dependent thermal-conductivity maps are shown in Figure S7. Compared with the thermal grease, the thermal pad exhibits more pronounced low-conductivity regions. We attribute these regions mainly to trapped air or locally insufficient contact, which are more likely to persist in the thermal pad because of its lower flowability. During the loading process, the overall thermal conductivity does not show an obvious pressure-dependent

trend, suggesting that compression within the investigated pressure range does not significantly alter the bulk heat-conduction pathways in the pad. However, the low-conductivity regions show local redistribution during compression, which may be associated with pressure-induced deformation and rearrangement of trapped air or imperfect contact regions.

During unloading, the thermal conductivity of the thermal pad gradually decreases, accompanied by a noticeable increase in low-conductivity regions. This behavior may be related to partially irreversible deformation and contact degradation, which can promote local air gaps or insufficient contact upon pressure release. These results indicate that, although the thermal pad has a more stable shape than thermal grease, its local thermal transport can still be strongly affected by compression history and contact evolution.

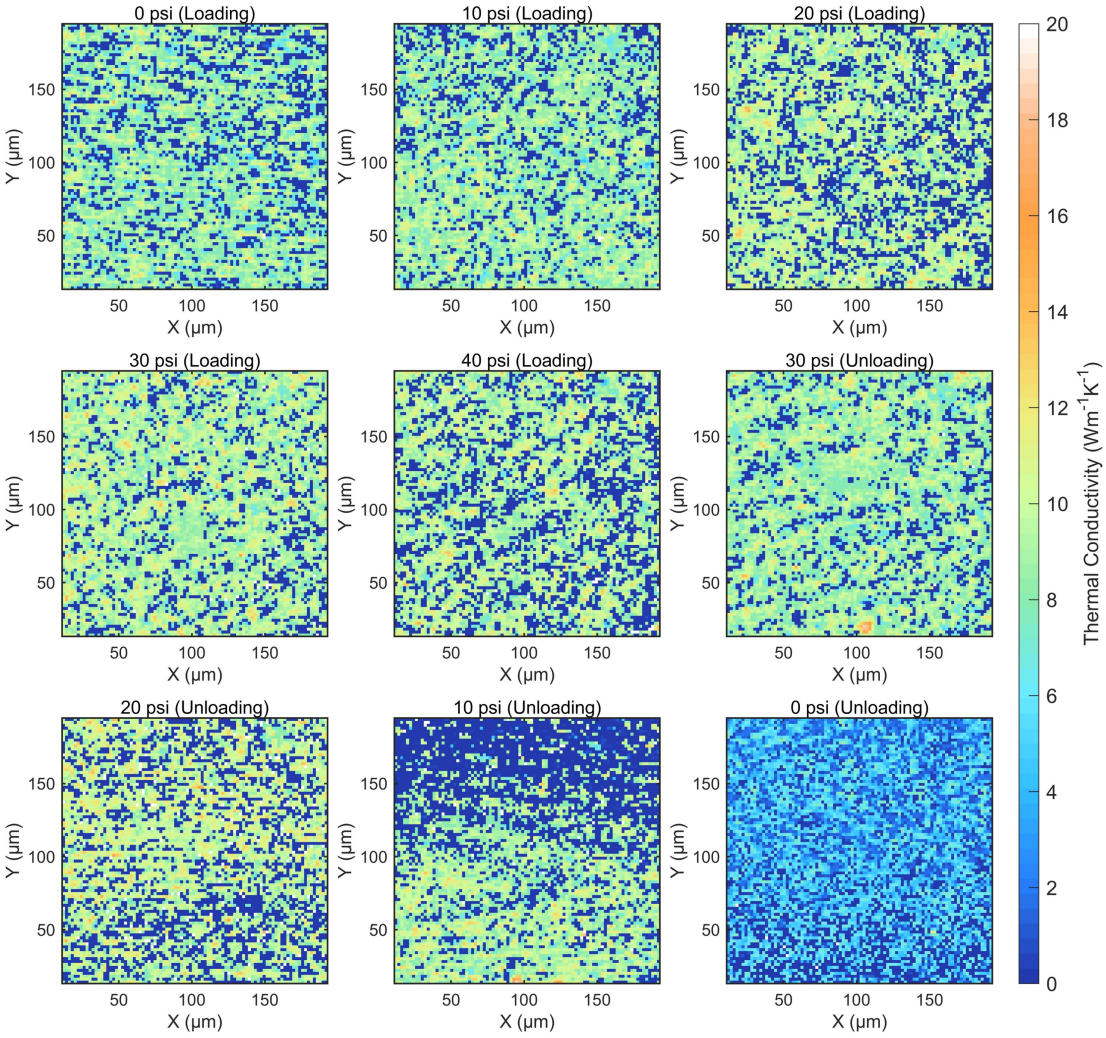

Figure S7. (a) Thermal conductivity and (b) interfacial thermal conductance maps of thermal pad at different contact pressures during loading and unloading processes.

S6.4 Statistical distributions under different pressures

The statistical distributions of local thermal conductivity under different contact pressures are shown in Figure S8. For the thermal grease, the distributions remain asymmetric with a long tail during both loading and unloading. The thermal pad also exhibits a long-tailed conductivity distribution, with more pronounced low-conductivity regions due to its lower flowability and the possible presence of trapped air or locally insufficient contact.

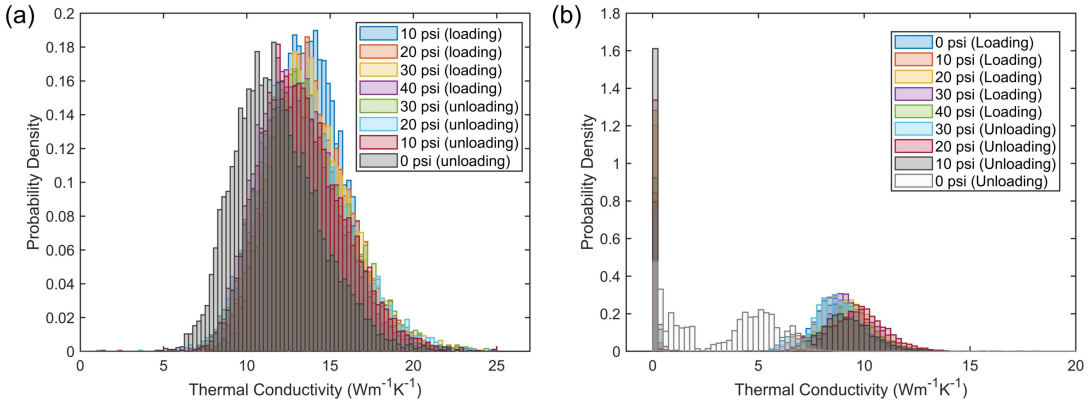

Figure S8. Thermal-conductivity distributions of (a) the thermal grease and (b) the thermal pad during loading and unloading.

S7.Fitting of Thermal Conductivity Distribution via the Proposed Model

In order to explain the origin of the thermal conductivity distribution, a statistical model is proposed in this work. Table S2 shows the related parameters for calculating the thermal conductivity distribution using the proposed model, where w_0 is effective radius, k_{m} and k_{p} are the thermal conductivities of the matrix and Al_2O_3, respectively, μ_r is the mean of $\ln R_{\mathrm{p}}$, σ_r^2 is the variance of $\ln R_{\mathrm{p}}$, R_{p} is the radius of the nearest-neighbor particle, λ is spatial number density of the particles. Here, λ, μ_r and σ_r are fitting parameters, with best-fit values listed in Table S2. Notably, the L1 region displays a distinct bimodal distribution: the primary peak at extremely low conductivity is attributed to macroscopic pores that induce a sharp reduction in heat transport, while the secondary peak represents domains with partial pore infiltration, manifesting intermediate conductivity between pore and the composite average. By incorporating a log-normal term to account for the attenuation effects induced by these defects, we achieved a robust fit for the L1 region's thermal conductivity distribution.

Table S2. Parameters for calculating the thermal conductivity distribution.

	w_0	k_m	k_p	λ	μ_r	σ_r
Units	μm	W $m^{-1}K^{-1}$	W $m^{-1}K^{-1}$	μm^{-2}	μm	μm
Overall	1.6	1[4]	30[5]	3.820	0.090	0.090
H1	1.6	1	30	4.745	0.147	0.088
L2	1.6	1	30	4.452	0.060	0.087

References

1.Sugawara A. The precise determination of thermal conductivity of pure fused quartz. J Appl Phys. 1968;39(13):5994–5997. [DOI:10.1063/1.1656103]

2.Brückner R. Properties and structure of vitreous silica. I. J Non Cryst Solids. 1970;5(2):123–175. [DOI:10.1016/0022-3093(70)90190-0]

3.Lovell S, Rollinson E. Density of thin films of vacuum evaporated metals. Nature. 1968;218(5147):1179–1180. [DOI:10.1038/2181179a0]

4.Liu Y, Li J. A protocol to further improve the thermal conductivity of silicone-matrix thermal interface material with nano-fillers. Thermochim Acta. 2022;708:179136. [DOI:10.1016/j.tca.2021.179136]

5.Yan X, Martin-Gonzalez M. Strategies for enhancing thermal conductivity of PDMS in electronic applications. Adv Mater Technol. 2026;11(4):e01210. [DOI:10.1002/admt.202501210]